Batteries & Supercaps

Research Article
doi.org/10.1002/batt.202500292

Chemistry Europe
European Chemical Societies Publishing

www.batteries-supercaps.org

Human-Centered Holographic Assistant using Computer Vision to Interact with Battery Manufacturing Machinery in a Predictive Manner

Diego E. Galvez-Aranda, Soorya Saravanan, and Alejandro A. Franco*

This work focuses on a novel human-centered digital assistant combining Mixed Reality (MR), Computer Vision, and Machine Learning regression to guide professionals and students on how to operate and correctly parameterize battery manufacturing machinery. This article aims to provide a proof of concept of the digital assistant, for a process involving an operator interacting with a semi-manual electrode calendering machine and examining how the intended calendering parameters will impact the electrode properties after calendering. The operator performs his/her actions while the digital assistant automatically detects the parameters entered by him/her on the machinery. Then, the digital assistant provides real-time predictions to the operator, helping him/her in decision-making through a minimalistic holographic interface minimizing visual hindrance. The ergonomics of the solution is optimized by acquiring feedback from users with various experience levels and evaluating their performance. As the necessity for advanced energy storage solutions rises, there is a strong need for modern training and guidance tools that aid in complex battery manufacturing processes at the prototyping stage, involving both semi-manual and automatic activities. Thanks to MR, the digital assistant has strong potential to improve manufactured electrode and cell qualities by emphasizing the egocentric perspective along the battery cell prototyping process.

1. Introduction

Rechargeable electrical energy sources, particularly lithium-ion batteries (LIB), play a pivotal role in addressing the global demand for sustainable and efficient energy solutions.[1–3] As a backbone of renewable energy integration and electric mobility, LIBs are essential for reducing carbon emissions and fostering a cleaner, more sustainable future.[4] In Europe, significant investments are being made in energy storage development, with initiatives aimed at expanding battery production capabilities and enhancing grid stability to support the growing reliance on intermittent renewable energy sources.[5,6] Battery gigafactories are becoming increasingly vital as the demand for electric vehicles surges. To meet the challenging targets of battery production, it is necessary to meet the labor demands. These demands can be fulfilled by providing specialized programs for battery education and reskilling workers from other fields, such as mechanical engineering, or other production industries (e.g., paper, food). To properly educate students and train workers, it is important to focus on guidance and training protocols.[7,8] In our previous works, we have reported innovative training of students and professionals with Virtual Reality (VR) serious games, allowing them to interact in an immersive fashion with battery materials, electrodes, cells, and manufacturing pilot lines.[7,9–11] We have also reported the innovative use of Mixed Reality (MR) to provide interactive holographic visualizations, directly in the place of experimentation, of electrode microstructures virtually produced in a VR battery manufacturing pilot line.[7] As previously reported in our publications, we found that these tools allow the workers and students to be more familiar with the complexity of battery technology and the related manufacturing process.[12]

However, during actual battery prototyping activities, workers can also benefit from MR technologies to guide them through their optimization tasks. In that sense, we have reported a MR holographic notebook designed to allow the battery experimentalist to collect, hands-free, the data he/she is producing while manufacturing battery electrodes.[12] This MR tool helps battery experimentalists to make informed decisions and has been found

D. E. Galvez-Aranda, S. Saravanan, A. A. Franco
Laboratoire de Réactivité et de Chimie des Solides (LRCS)
Université de Picardie Jules Verne
Hub de l'Energie
UMR CNRS 7314
15 rue Baudelocque, 80039 Amiens Cedex, France
E-mail: alejandro.franco@u-picardie.fr

D. E. Galvez-Aranda, S. Saravanan, A. A. Franco
Réseau sur le Stockage Electrochimique de l´Energie (RS2E)
FR CNRS 3459
Hub de l'Energie
15 rue Baudelocque, 80039 Amiens Cedex, France

A. A. Franco
ALISTORE-European Research Institute
FR CNRS 3104
Hub de l'Energie
15 rue Baudelocque, 80039 Amiens Cedex, France

A. A. Franco
Institut Universitaire de France
1 rue Descartes, 75231 Paris Cedex 05, France

Supporting information for this article is available on the WWW under https://doi.org/10.1002/batt.202500292

Research Article
doi.org/10.1002/batt.202500292
Chemistry Europe
European Chemical Societies Publishing

to increase work efficiency, reducing errors and accelerating skill development. This is achieved through reducing the time required to collect and analyze data, providing instructions to follow, and through an enhanced ability to look at the expected results.[12]

Four paradigms exist in the state of the art to optimize battery manufacturing processes (**Figure 1**). However, none of them is suitable to assist in a predictive and ego-centric fashion an operator or trainee in the semi-manual and manual activities he/she undertakes in a battery prototyping process.[13]

A first paradigm, based on a trial-and-error experimental approach, driven by the experimentalist intuition,[14] was soon followed by a second paradigm, an experimental approach based on design-of-experiments,[15] allowing to perform "systematic manufacturing/performance relationships characterizations" in a screening fashion. Later, our ARTISTIC project initiative[13] introduced a third paradigm: the assistance of experimental optimization along the whole battery manufacturing process by results obtained from digital models of the main machinery-level manufacturing steps. These digital models rely on physics-based numerical models and AI/Machine Learning (ML) models. While the former describes the physics going on along the process in the form of mathematical equations that are solved numerically, the latter are based purely on data, establishing correlations between manufacturing inputs and output properties. They assist in the choice of a set of manufacturing machinery parameters through the prediction of the process parameters' influence on electrode and cell properties. They concentrate on the production scale with wet electrode processing, that is, on the parameters that are controlled through the different machines involved in the manufacturing process based on wet electrode processing (e.g., coating speed, comma gap, slurry drying temperature, and calendering pressure). AI/ML models were trained with experimental data from our prototyping line and with synthetic data arising from physics-based manufacturing simulations. The models can predict how the chosen manufacturing parameter values (e.g., calendering pressure) impact the electrode properties (e.g., porosity, conductivity).[16–24] We can also leverage a transfer learning approach to train models when only a small dataset is available. We have demonstrated this concept by initially training a neural network on a large dataset and then transferring its architecture to a smaller dataset by adding an additional artificial neural layer for fine tuning.[25] This innovative approach was validated using existing experimental manufacturing and stochastically generated datasets.

The integration of AI/ML models in a Bayesian optimization loop made possible the first demonstration of an inverse design concept (i.e., predicting which manufacturing values to adopt to obtain the desired electrode and cell properties, e.g., electrode with maximal conductivity and minimal tortuosity).[26,27] Other works also report physics-based numerical models to simulate electrode drying and calendering, but do not consider explicitly the carbon and binder.[28,29] Other ML models assess the impact of coating conditions on electrode properties and use Explainable AI (XAI) to interpret the results.[30,31] This third paradigm is carried out without real-time coupling between models and machinery, that is, the results of the modeling (e.g., prediction of optimal slurry formulation and calendering degree) are injected manually by experimentalists in their workflow (e.g., to adjust the machinery parameters values).

The fourth paradigm is the one intending to couple in real time the manufacturing machinery with the digital models providing instructions to the machinery on how to autonomously optimize the manufacturing process. The latter constitutes the concept of the digital twin. In this concept, sensors are being used in real production machines collecting data in real-time (e.g., the thickness of the electrodes being produced, the areal homogeneity of the electrodes).[13,32] The collected data is continuously fed into an AI-empowered digital model processing it in real time and giving instructions via actuators to the machines to improve, in an autonomous way, the undergoing process (e.g., adjusting the slurry drying temperature to improve the homogeneity of the produced electrodes). Autonomous laboratories start to emerge following this concept for high-throughput materials synthesis and characterization.[33–38] This digital twin concept, intended by some battery Gigafactory companies, is mainly useful to reduce production scraps in the pilot line and factory stages, which are the ones having the highest degree of machinery automation. These efforts actually consist of providing intelligence to the machines involved in the manufacturing process, to

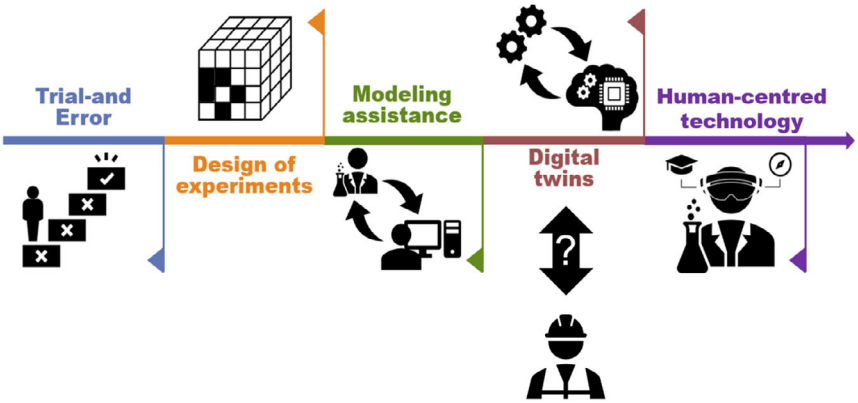

Figure 1. The four state-of-the-art paradigms (Trial and error, Design of experiments, Modeling assistance, and Digital twins) to optimize battery manufacturing processes. Our human-centered technology introduces a new approach.

make them autonomous, minimizing the human place in the loop.[32] While digital twins can be useful in a pilot line or production scale, where scraps come from un-optimal processability conditions, machinery failure, and mass production statistics, they are not useful to support, in a predictive and egocentric fashion, an operator or trainee in his/her undergoing semi-manual and manual interventions in a battery prototyping process.[13] An example of activity in the prototyping stage is the electrode calendering process (**Figure 2**). One of the simplest calendering machines requires the user to manually adjust the appropriate roll gap, temperature, and speed of the machine according to the input electrode properties, and then manually feed the electrode deposited on a current collector to the calendering machine (Figure S1, Supporting Information). Once the electrode is calendered, the user takes it out from the machine and measures the thickness to determine the electrode porosity.

In the battery manufacturing industry, Computer Vision (CV) is becoming an important tool, focusing particularly on automating quality control and optimizing production processes at the machinery level.[39] One key application is in postprocess labeling—a task that involves inspecting the batteries for defects, ensuring correct labeling, and verifying that the cells are appropriately packaged. For example, CV systems can identify and flag defects such as surface cracks or incorrect labeling.[38,40–43] These systems use high-resolution cameras combined with ML algorithms to accurately detect even the smallest inconsistencies, promising to ensure that only defect-free electrodes and cells reach the market. By automating these quality checks, manufacturers can reduce human error, increase throughput, and minimize waste.

In summary, the scientific methodology for battery manufacturing optimization has been evolving from a human-centered activity to one centered on machinery. In this article, we propose a new technology that turns this around, introducing a groundbreaking human-centered (or egocentric) digital assistant designed for MR glasses, which harnesses advanced CV algorithms together with ML-based real-time prediction to support and guide battery prototyping activities involving semi-manual operations (**Figure 3**). This innovative solution seamlessly integrates real-time data acquisition from a calendering machine through the human user's MR glasses camera, processed by a CV approach. The collected data from the human field of view is then used to make a real-time prediction of the calendered electrode porosity as the calendering process is happening. This application empowers human battery experimentalists with actionable insights, paving the way for smarter, more efficient battery prototyping. Through this new technology, we aim to redefine how stakeholders engage and optimize their manufacturing processes in an increasingly competitive landscape. We demonstrate our tool here with Microsoft HoloLens MR glasses (HL) as proof of concept, without excluding its transferability to other MR hardware technologies. Equally, our technology can be extended to other battery prototyping steps. Our article is organized as follows. First, we present the workflow composed of four stages (data collection, data processing, data prediction, and data display), going into detail through each of these stages. Then, a description of the dataset preprocessing is presented so that the digital assistant is ready. This includes the training dataset for the ML model and the digital assistant program flowchart. Next, we describe the usage scenario and preliminary results based on testing scores. Finally, we provide a summary and outlook of our work.

2. Methodology

In terms of the required hardware, our digital assistant is supported on HL glasses, a server, and a mobile phone. In the following, we present our dynamic computational workflow that

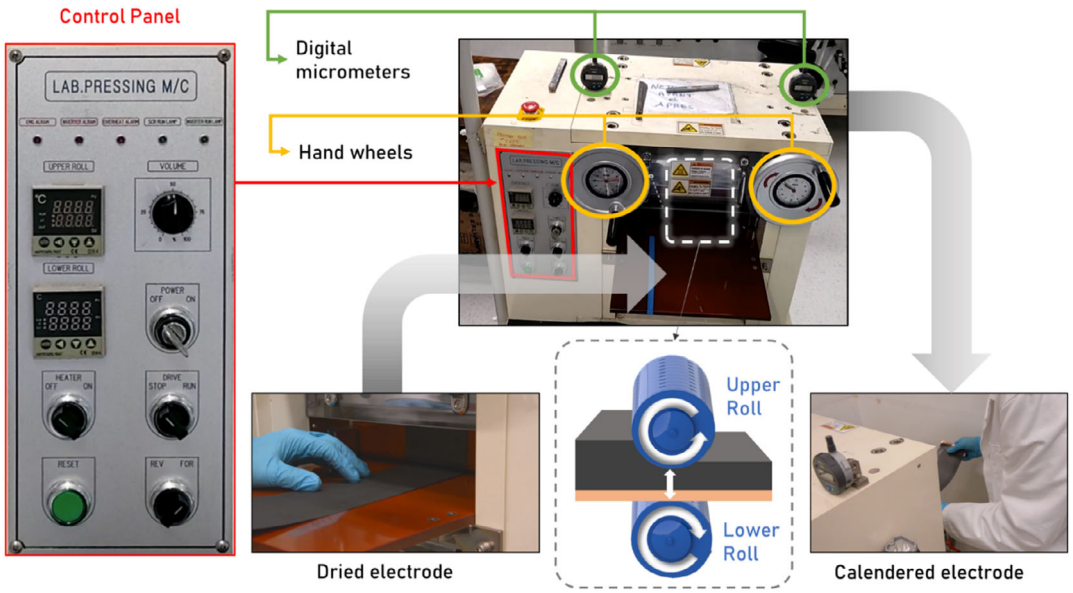

Figure 2. Calendering electrode manufacturing process and machinery. The control panel sets up the temperature of the upper and lower roll, the direction of the linear motion when the electrode enters the roll gap (forward or reverse), and the activation or not of the heater. The roll gap is calculated from the values of the two digital micrometers located at the top of the calendering machine. The dried electrode is inserted into the gate at the front of the calendering machine, and the calendered electrode is collected from the back of the calendering machine.

Research Article
doi.org/10.1002/batt.202500292
Chemistry Europe
European Chemical Societies Publishing

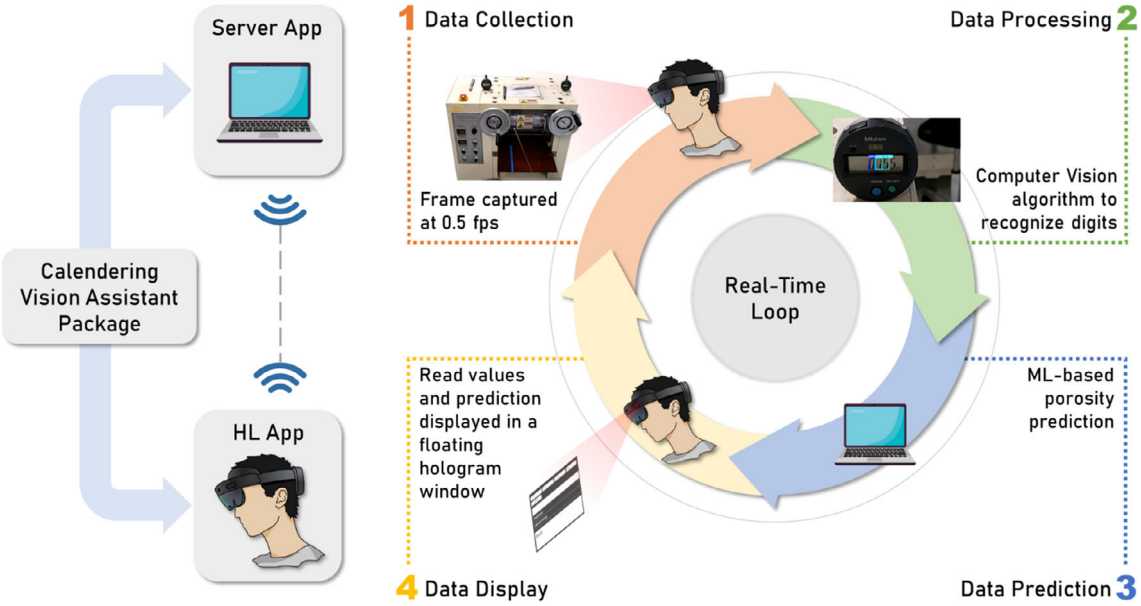

Figure 3. Workflow of our real-time prediction of electrode properties using computer vision for automatic recognition of the parameters entered by a user in a calendering machine.

provides a user's egocentric experience. An important aspect to provide a seamless user experience is a fluent data exchange between the server application and the two client devices (HL and mobile phone). Once the connection between the three of them (server, HL, and mobile phone) is established, and the application (App) is executed from the HL, the real-time processing loop starts working. This real-time processing loop consists of four distinct stages that continuously execute at fixed intervals. This structured approach ensures that data is consistently updated and synchronized between the HL app and the server app, allowing real-time interactions and responsiveness (Figure 3).

Stage 1 involves the collection of data, which comes from two sources: from HL for visual environmental information and from the mobile phone, the latter used to enter the parameters describing the dried electrode (mass loading, active material content, active material type, and initial thickness). The collected data is then transmitted from both devices (HL and mobile phone) to the server. In stage 2, the server App performs the corresponding CV computation to collect information from the user's visual environment. At stage 3, an ML model, previously trained, performs the calculations to predict the calendered electrode porosity by using all the collected data (from Stages 1 and 2). Stages 2 and 3 are executed on the server. Once stage 3 is completed, the server sends the results to HL to start stage 4. It is important to mention that the HL–server communication involves the exchange (send/receive) of information. However, the mobile phone–server communication is only in one direction, that is, the mobile phone only sends information to the server. At stage 4, the HL acts on the server's response, updating the holographic user interface to display the collected and predicted data. This cyclical flow of data exchange between stages 1 and 2, and then between stages 3 and 4, establishes a robust framework for continuous interaction and ensures that both HL and server remain synchronized throughout the application's runtime.

2.1. Data Collection: Frame Storage

At this stage, we collect images from our environment while the user is manipulating the calendering machine. We capture images (frames) from the HL video feed at a rate of 0.5 frames per second (fps). We utilize the OpenCV[44] Python library to get the frames that we will further process. Each frame is processed at a resolution of 1920 × 1080 pixels, allowing for efficient data handling while maintaining adequate detail for analysis. The HL transmits the frames to the server, where they undergo further examination by our CV system to extract values of four displays as described below.

The model is designed to collect a total of eight input variables. Three of these inputs are provided through the mobile phone device (mass loading, active material content, and initial thickness), with the active material type ($LiNi_{0.33}Mn_{0.33}Ni_{0.33}O_2$, here on referred to as NMC111) being another input that can be handled (not changed in this study). The remaining four input variables are obtained via a computer vision approach by analyzing the image captured by the HL (left micrometer, right micrometer, upper temperature, and lower temperature). The output of the model consists of a single variable (the predicted porosity), which is computed based on the combined information from both mobile device and computer vision sources, as explained in the upcoming sections.

2.2. Data Processing: Computer Vision

Our CV system automatically recognizes, from an egocentric (human-centered) perspective, the following four input parameters present on the machine displays: upper and lower rolls' target temperatures and left and right digital micrometer values. The CV algorithm utilizes a three-stage approach to effectively

Research Article
doi.org/10.1002/batt.202500292
Chemistry Europe
European Chemical Societies Publishing

read the numerical values displayed on the corresponding four distinct displays (**Figure 4**). At the first stage, the algorithm focuses on object recognition, identifying the front panel (for roll temperature reading purposes) and the top digital micrometers (for roll gap reading purposes). This step is crucial as it ensures the algorithm accurately locates the relevant displays within the broader context of the calendering machine. Once the object is recognized, the second stage involves identifying the specific display areas themselves. Lastly, at the third stage, with the display regions pinpointed, the algorithm then employs digit recognition techniques to interpret the individual numbers shown on the displays, thereby extracting the precise numerical values. At each stage, the segmented figure is increased twice in size to decrease potential error in the CV recognition algorithm. This systematic approach not only enhances accuracy but also streamlines the process of retrieving vital data from the calendering machine.

We employ the YOLO[45] framework to train our CV system, leveraging its ability to perform object detection in real time. To achieve an optimal balance between accuracy and prediction processing speed, we have chosen to utilize the medium-sized model (41 MB) for object and display detection, and the large-sized model (90 MB) for digits detection. This model offers a compromise that enhances detection performance without sacrificing the rapid processing times essential for our real-time digital assistant.

For each object, we have generated training datasets using augmentation methods to enlarge the dataset, ensuring adaptability to the different lighting conditions we can find in our real environment (Figure S2, Supporting Information). We augmented the training data by creating darker and lighter variations of the original images. This approach ensures that variations in lighting conditions within the room do not adversely affect the recognition of objects and digits. Then, we proceed to annotate the images by labeling the different objects we want the CV to identify.

Additionally, and only for the LED green display digits detection, we implement an additional step: the application of a green filter on the images. The digits from the green LED display corresponds to the target temperature that is set by the operator. The digits from the red LED display corresponds to the actual temperature of the rolls. We only consider the target temperature value since it is the temperature the operator wishes to operator the machine, and therefore requires the property prediction for operation at that temperature. This filter is critical as it ensures that only green LED light is captured during the training and future real-time application process. By isolating the green LED light, we effectively eliminate potential noise that could arise

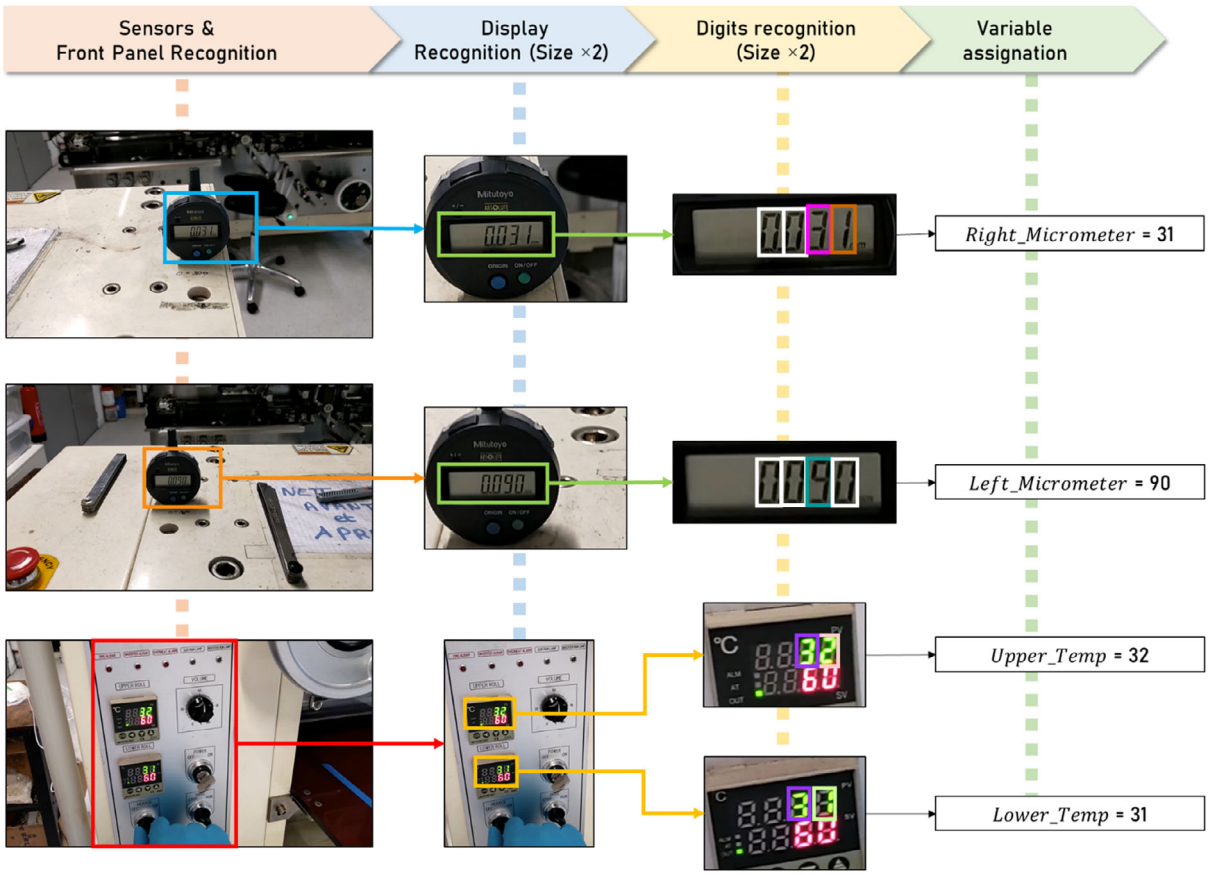

Figure 4. Workflow of data processing using CV to recognize the four values from the calendering machine displays: left digital micrometer, right digital micrometer, upper roll temperature, and lower roll temperature. Each color represents a pre-trained object: control panel (red), left digital micrometer (orange), right digital micrometer (light blue), digital micrometer display (green), LED temperature display (yellow), and different colors for all the digits from 0 to 9.

from the red LED light, which may interfere with the accuracy of digit detection. This targeted filtering enhances the clarity of the images, allowing the model to focus solely on the relevant digits of the green LED display.

Five different models were trained, and each of them is used at different stages of the CV recognition process (Figure 4). At the first stage, Micrometer & Front Panel Recognition, the Machine Devices model is used. At the second stage, Display Recognition, the Temperature Display and Digital Micrometer Display models are used. Finally, at the third stage, Digits Recognition, the Micrometer Digits and LED Green Digits models are used. The details regarding the number of images used to train each model are listed in **Table 1**.

2.3. Data Prediction: Porosity

The data prediction model utilizes a total of five input variables to forecast the calendered electrode porosity. Among these, three variables are entered by the user through a mobile phone interface prior to the calendering process, allowing for personalized settings based on the material used for the electrode (Figure S3, Supporting Information). These three variables are mass loading (m_l) in mg cm^{-2}, active material content (AM_c) in weight fraction, and initial thickness (Th) in μm. The remaining two variables are process parameters of the calendering machine, namely the roll temperature (Temperature) in °C, and roll gap (Roll_Gap) in μm. The effect of roll speed is not considered here since its effect is reported to be statistically insignificant and is usually kept constant during operation.[19] The different process parameters are dynamically collected during the calendering operation, thanks to our CV recognition system, and can vary in real time as the user interacts with the calendering machine. The calendering machine used in the current work is a prototype-grade lap press calender (BPN250, People & Technology, Korea).

Table 1. Training datasets per model for our CV system detection.

Model	Original number of images	Total images after augmentation	Object	Object quantity
Machine Devices	180	540	Front Panel	180
			Left micrometer	210
			Right micrometer	210
Temperature Display	80	240	Temperature Display	240
Digital Micrometer Display	50	150	Micrometer Display	162
Micrometer Digits	40	120	0	20
			1	20
			2	15
			3	17
			4	20
			5	20
			6	21
			7	22
			8	24
			9	23
			–	20
LED Green Digits	32	96	0	18
			1	20
			2	22
			3	21
			4	21
			5	25
			6	19
			7	18
			8	21
			9	22

The calendering machine consists of a control panel where the process steps, temperature, speed, and direction of the calendering process are controlled (Figure 2). The front of the calendering machine contains two hand wheels, which allow the operator to control the initial roll gap precisely. The top of the calendering machine contains two digital micrometers, which allow the operator to check the displacement of the calender rolls. To perform the calendering operation, the operator has to calibrate the roll gap with a 300 μm gauge, after which the micrometers are set to zero. Then, the operator has to set the desired temperature of the rolls. Once the temperature is reached, the operator sets the roll gap of the machine by using the two hand wheels. The operator needs to make sure that both the digital micrometers show the same value, during both the calibration step and the setting step, to ensure correct alignment of the calendering rolls. As the initial roll gap is set at 300 μm and the digital micrometers are set to zero, the operator needs to reduce the roll gap until the desired roll gap is reached. Finally, the operator set up the direction and speed of the roller. The roll gap set by the operator starts deviating from the actual roll gap once a critical value of the pressure exerted by the calendering rolls on the electrode is reached. The roll gap after which the deviation starts depends on the mass loading and AM content of the electrode. Here, the term roll gap is defined as the gap between the rolls that was set by the operator before the calendering process.

To proceed with the prediction, the operator needs to check the alignment of the rolls. This is ensured by having the same value of the distance moved by both sides of the roller in the digital micrometers of the calendering machine. Then, the average of the values is automatically calculated to estimate the roll gap that will be used for the prediction. Since the rolls also have individual temperature control, the average temperature of both rolls is taken to be the roll's temperature during the calendering process. Therefore, during the calendering operation, a total of four values are obtained from our CV object detection algorithm. These four values are as follows: upper roll temperature (Upper_Temp) in °C, Lower roll temperature (Lower_Temp) in °C, Left roll gap (Left_Micrometer) in μm, and right roll gap (Right_Micrometer) in μm. From the initial four variables gathered during the operation, we calculate the absolute temperature

Research Article
doi.org/10.1002/batt.202500292
Chemistry Europe
European Chemical Societies Publishing

(Temperature) and the average roll gap (Roll_Gap) using the following formulas

$$\text{Temperature} = \frac{(\text{Upper\_Temp} + \text{Lower\_Temp})}{2} \quad (1)$$

$$\text{Roll\_Gap} = \frac{[(\text{Left\_Micrometer} + 300) + (\text{Right\_Micrometer} + 300)]}{2} \quad (2)$$

Once the roll gap values and temperature values are available, the final porosity is calculated. For the calculation of the final porosity, we use an ML model trained from experimental data previously acquired in our research group.[13,19,46] The acquired raw data has parameters with strong correlations among each other, like mass loading, initial thickness, and roll gap. To reduce this inherent dependence, these are converted to more independent parameters: initial porosity, compression degree, and final porosity. Here, the compression degree is defined as

$$\text{Compression Degree} = \frac{\text{Th} - \text{Roll\_Gap}}{\text{Th}} \quad (3)$$

The resulting distribution of the dataset used and the correlation matrix are provided in Figure 6. However, some undesirable correlations still occur due to the inherent process requirements while preparing electrodes for various purposes (**Figure 5**a). For example, the collected data arises from experiments done for optimizing industrially relevant formulations of electrodes. These electrodes are prepared to have higher mass loading and higher AM contents, compared to those collected from experiments designed to understand AM performance only. Also, a correlation between initial porosity and the mass loading naturally exists because of the drying process. During this process, using low-coating comma gaps results in electrodes with lower mass loading and higher porosity, resulting in a notable inverse correlation between mass loading and porosity in the acquired data.[47]

The distribution of the data is also skewed across the features (Figure 5b). The raw data was observed to have features mainly in the higher values of the compression degree. This results in the final porosity value mainly in the low porosity region. So, to improve the distribution, additional data points were created considering zero compression degree since it is known that without calendering, the final porosity remains the same as the initial porosity. Having a more uniform distribution enables us to reduce bias, improve generalization, and ensure more reliable model performance across diverse scenarios in machine learning. However, the distribution is not completely uniform since the data is collected from experiments from different use cases. Since our goal is training new operators to match experienced operators' results, the current distribution representing experienced operators' values is adequate for training an ML model to accomplish this task.

To predict the final porosity from the input parameters, a random forest regression model is use with tools from Python's Scikit-learn library.[48] A dataset consisting of 293 data points made up of the five manufacturing parameters is used to train the model. A random forest regressor is chosen so that the model can reflect the nonlinear relationship of the inputs and the target variable while being less data hungry than a Neural Network. The data is split into 80–20% for model training and testing, respectively. Since we have a non-uniform distribution of the target variable in our dataset, a stratified split is obtained for the numerical target values to have a better distribution of the training and testing data. The grid search cross-validation algorithm is used to systematically evaluate and identify the optimal hyperparameters for the model. And Stratified K-fold cross-validation with five folds is performed to assess the best model's performance with different sets of training data while maintaining the target variable's distribution in each fold.

2.4. Data Display: Holographic Interface

Our App consists of three different modes: HOME, START, and ZOOM. The user can navigate through these three modes by pressing their corresponding button in a control panel displayed

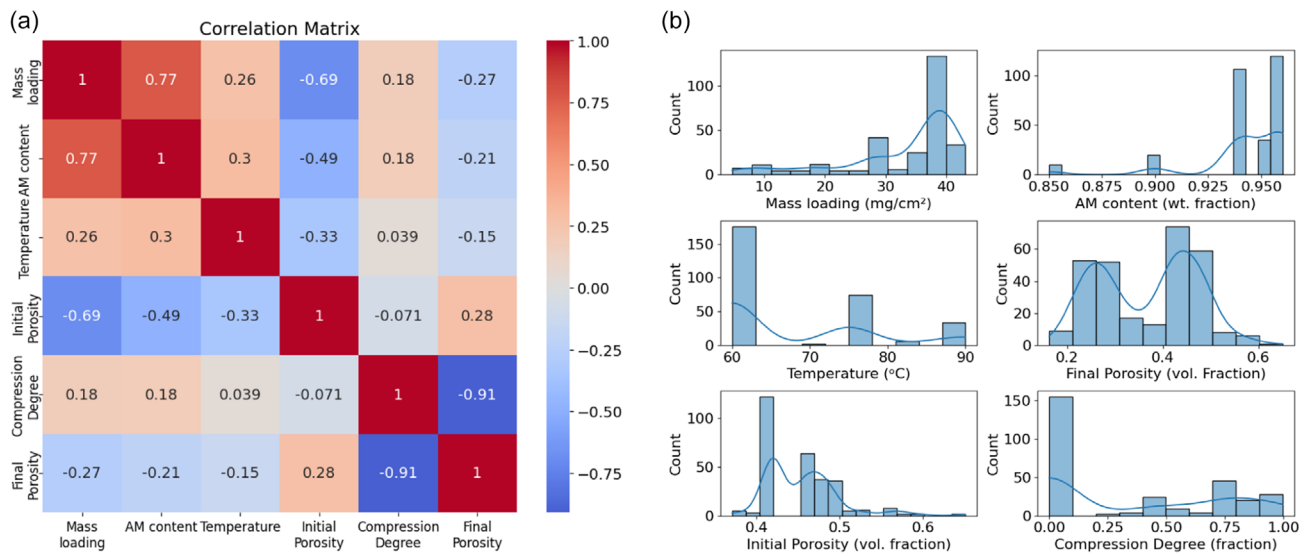

Figure 5. a) Correlation matrix of treated data. b) Data distribution after preprocessing and data augmentation steps.

Research Article
doi.org/10.1002/batt.202500292
Chemistry Europe
European Chemical Societies Publishing

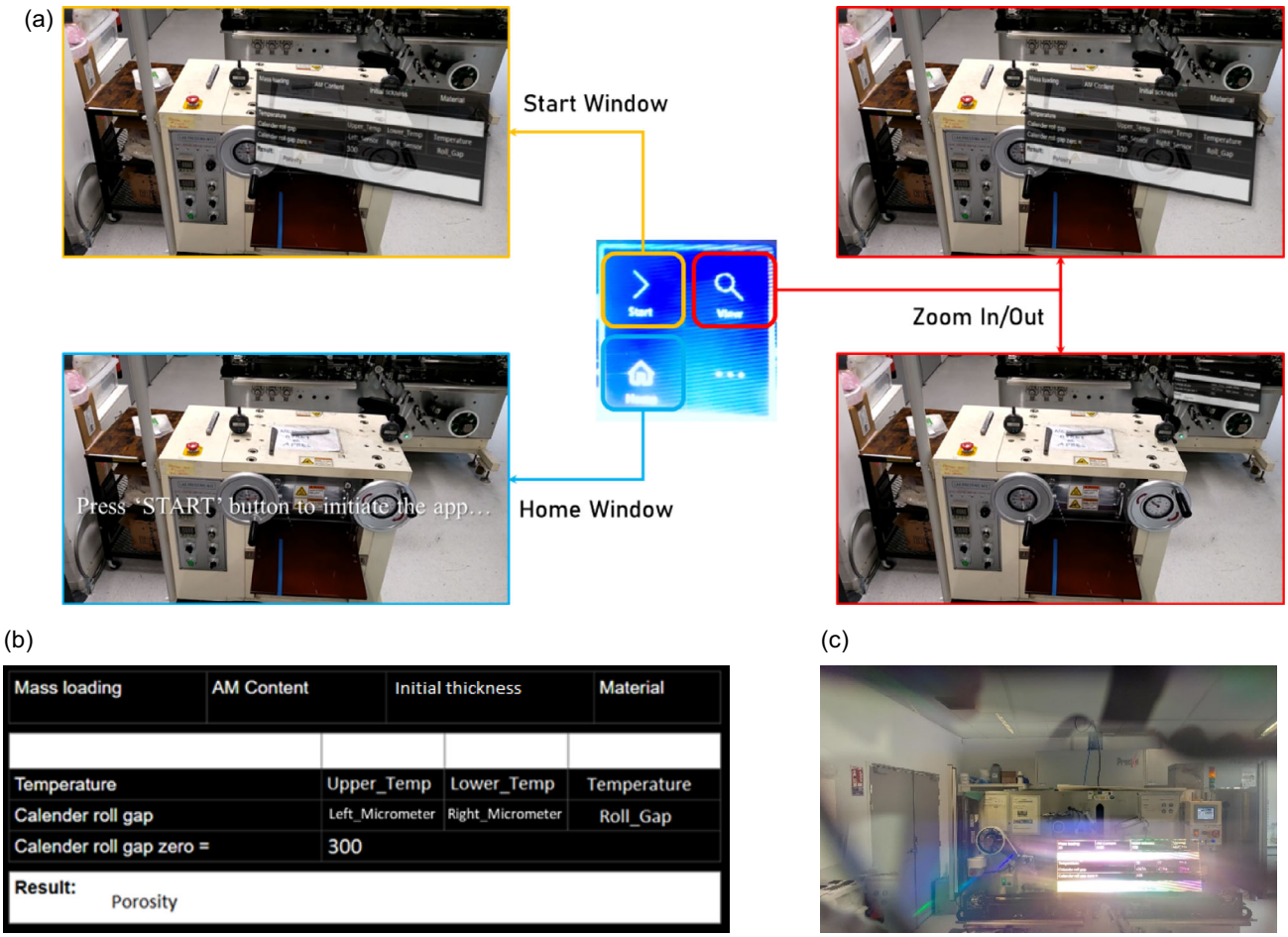

Figure 6. a) Navigation along the different windows of the holographic interface. b) Holographic display showing the variable values during the calendering process. c) Real view of the holographic window by the user from the HL field of view. The video recording feature of the HL is locked while our App is working, since we use that feature to get the frames in real-time. Therefore, a video recording displaying the holographic window from an egocentric perspective is not possible via the HL; that is why we show only a photo here.

by moving the arm in front of the egocentric HL field of view (**Figure 6**a). Upon launching the HL App, the HOME window is displayed. In the HOME window, operators can see a welcome message and an indication to start the App by pressing the "Start" button visualized on a holographic control panel. Once the "Start" button is pressed, the START mode is activated, and operators can visualize an advanced holographic transparent panel displaying all input variables alongside the predicted porosity in real time (Figure 6b). This innovative interface allows users to monitor the temperature and roll gap parameters continuously, ensuring they remain informed about the current state of the calendering machine and how these intended parameters impact the electrode porosity (**Figure 7**b,c). The holographic display not only enhances operator engagement but also facilitates immediate decision-making, as the operator can visualize the intricate relationships between input variables and their influence on the predicted porosity. Finally, by pressing the "Zoom" button, the operator can zoom in and zoom out (ZOOM mode) the holographic panel to increase visibility when required.

As the operator interacts with the calendering machine, the temperature and roll gap variables are dynamically updated through a continuous feedback loop enabled by our CV system. This means that any adjustments made to the machine settings will be reflected instantaneously on the holographic panel, showcasing the corresponding changes in the predicted porosity. This real-time data visualization empowers operators to optimize their processes effectively, as they can quickly assess how each manipulation affects the quality and consistency of the calendered electrode.

2.5. Python Script

A Python script has been developed to collect data from the mobile phone interface, process the frame captured by the HL camera, make a prediction using our ML model, and show/update the predicted values in the holographic display. The main loop of the program consists of two functions: Process_Frame and Update_Display. The main loop is executed at a frequency of 0.5 s. The 0.5 s threshold is established as a value that will give enough time to finish the execution of the three functions before the arrival of the next frame. The Process_Frame function (Figure 7) starts by collecting the information input in the mobile phone and assigning them to the variables mass loading (m_1),

Research Article
doi.org/10.1002/batt.202500292
Chemistry Europe
European Chemical Societies Publishing

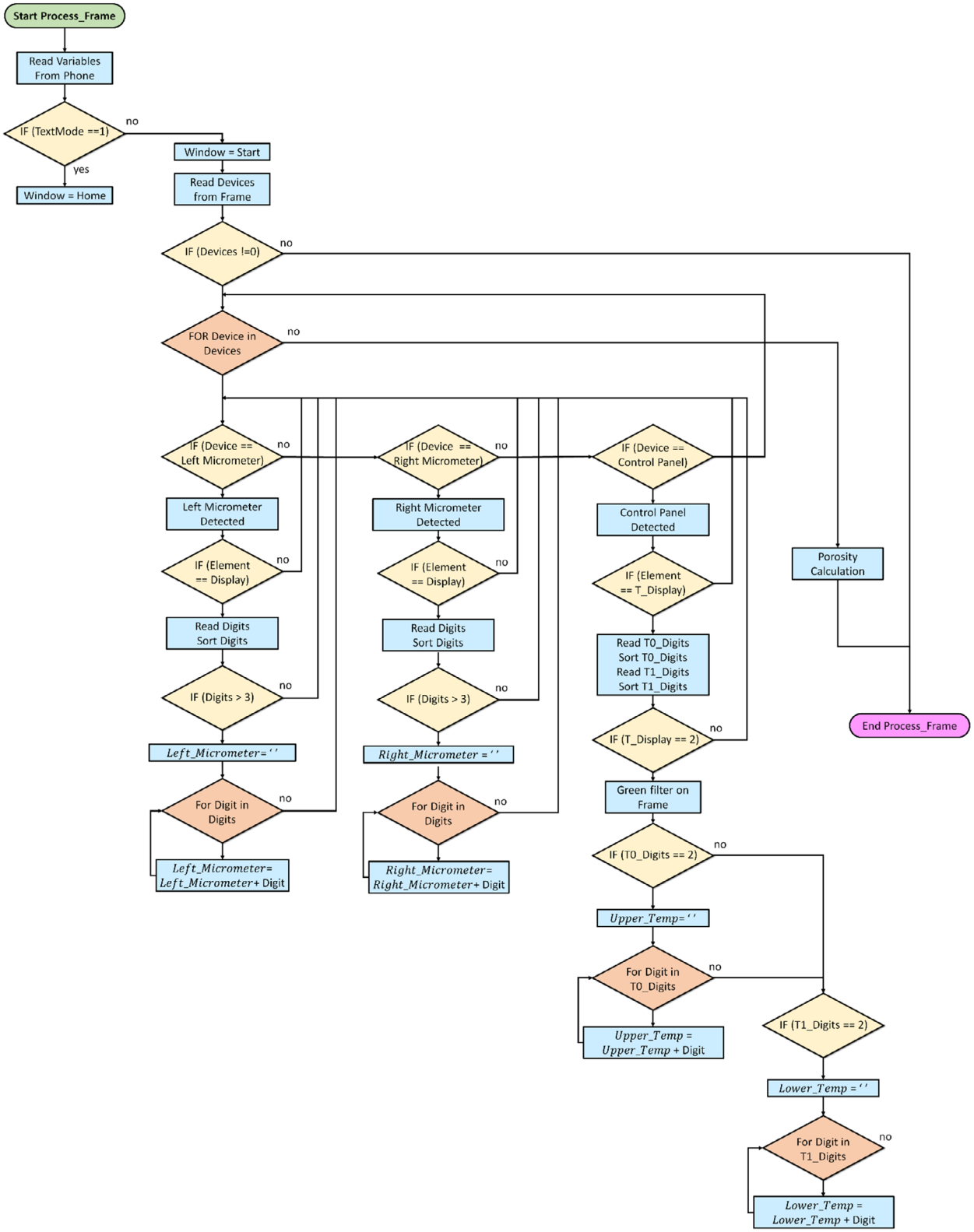

Figure 7. Flowchart of the Python script behind the *Process_Frame* function.

active material content (AM), and initial thickness (Th). Then, the function checks the value of the variable TextMode to identify if we are in the HOME window (TextMode = 1) or we are in the START window (TextMode = 0). If the START window is activated, then our CV algorithm is executed based on the trained models explained in Section 2.2. The CV algorithm recognizes any of the three devices (control panel, left and right digital micrometers) and stores them in the Devices array. A FOR loop is executed

searching for all the recognized Device in the Devices array. Three IF conditionals statements are implemented, each of them assigned to be executed when their corresponding device is recognized.

The first two IF conditional statements are designed to identify and get the values of the left and right roll gap digital micrometers. These two IF statements have the same programming structure. Once the micrometer is identified, the code enters a nested IF conditional statement to identify the corresponding micrometer display area. If the display area is successfully recognized (Element = Display), the digits displayed are identified. Therefore, the program proceeds to a final IF conditional statement that requires a minimum of four digits to be identified (Digits > 3). Finally, a FOR loop is utilized to aggregate the identified digits into the corresponding designated variable for each digital micrometer (Left_Micrometer and Right_Micrometer).

In contrast, the handling of the third device (control panel) involves a slightly different structure. The initial sub IF statement focuses on recognizing the two temperature displays located in the control panel (Element = T_Display). The code first checks for the presence of both displays (T_Display = 2). When both temperature displays are identified, then a green filter is applied to the captured temperature display images. The green filter ensures a better read of the green LED display, assessing the values of the digits from each temperature display sequentially. Therefore, the program proceeds to a final IF conditional statement that requires two digits to be identified per temperature display (Digits = 2). Finally, a FOR loop is utilized to aggregate the identified digits into the corresponding designated variable for each temperature display (Upper_Temp and Lower_Temp).

Following the completion of the main FOR loop (Device in Devices), which explores all identified devices, the program calculates the predicted porosity through our ML model, thereby concluding the Process_Frame function. Then the Update_Display function is called, which gets the values obtained from the first two functions (Input_Mobile and Process_Frame) and then updates the holographic interface, including the predicted porosity.

3. Results

3.1. Data Processing: Computer Vision

As described in Section 2.2, five different models were trained: the Machine Devices model (to identify Micrometers & Front Panel), the Temperature Display model, the Digital Micrometer Display model, the Micrometer Digits model, and the LED Green Digits model (Table 1). To train our CV algorithm, we prepared five distinct datasets to effectively train each of the previously listed models, ensuring a better approach to object identification. Since the CV algorithm has been developed using the YOLO library, it is essential to understand the distinctions between a box, a class, and an object. A "box" refers to the bounding box that delineates the spatial extent of an "object" within an image, while a "class" signifies the category or label assigned to that "object." Finally, the "object" denotes the actual instance of the "class" present in the image, which is what the model aims to detect and classify based on the training it has received. For example, an object "digit" can have 10 classes (from 0 to 9). Therefore, we trained three models focused on a multiclass detection (Machine Devices, LED Green Digits, and Micrometer Digits), and the remaining two models on single-object detection (Temperature Display and Digital Micrometer Display).

The three multiclass detection models are the following: Machine Device model which identifies the three devices from the calendering machine (control panel, left and right digital micrometer), LED Green Digits model which identifies the digits from 0 to 9 from the temperature display, and Micrometer Digits model which identifies the digits from 0 to 9 and the - symbol. In all three of these cases, we placed significant emphasis on maintaining a uniform distribution of training data across the different classes of each model (**Figure 8**a,g,i). By balancing the representation of each object class, we aim to prevent any potential bias and enhance the model's ability to generalize well across unseen data. The remaining two datasets focus exclusively on single-object detection tasks. In these scenarios, the model's objective is to accurately identify and localize a single specific object within an image. The Temperature Display model is trained to identify the temperature display in the control panel (Figure 8c). The Digital Micrometer Display model is trained to identify the micrometer display in the micrometer device (Figure 8e). To evaluate the model's performance and ensure that it is not overfitting to the training data, we plotted the validation (Figure 8b,d,f,h,j) and training loss curves (Figure S4, Supporting Information). The loss function is the mean square error (MSE).

3.2. Data Prediction: Porosity

The optimized model hyperparameters of the random forest regressor model are given in **Table 2**. The choice of these hyperparameters aims to control model complexity and potentially reduce overfitting. It is seen from Table 2 and **Figure 9**a that the model performance is very high. However, we should be cautious when using the model to make predictions with a low compression degree since we do not have a high distribution of training data in that range of parameter space. It can be used under the conditions of high compression degree, which provides the lowest porosities. The model is permitted to be used for this scenario since the model has greater uniformity in the higher ranges of this parameter space. Since the objective is to train professionals to perform experiments with high compression degrees during the calendering process, it is safe to assume that this model is effective for this use case. However, it is worth noting that more sophisticated ML models can be easily integrated into our digital assistant.

From the feature importance graph based on the absolute average SHAP values (Figure 9b), we see that the most impactful factor affecting the output porosity is the compression degree. The compression degree shows the highest importance since the compression degree is directly related to the pressure applied on the electrode. Various studies have also reported that the applied pressure has the highest effect on the final porosity of the electrode.[19] It can also be seen that AM content has a slight

Research Article
doi.org/10.1002/batt.202500292
Chemistry Europe
European Chemical Societies Publishing

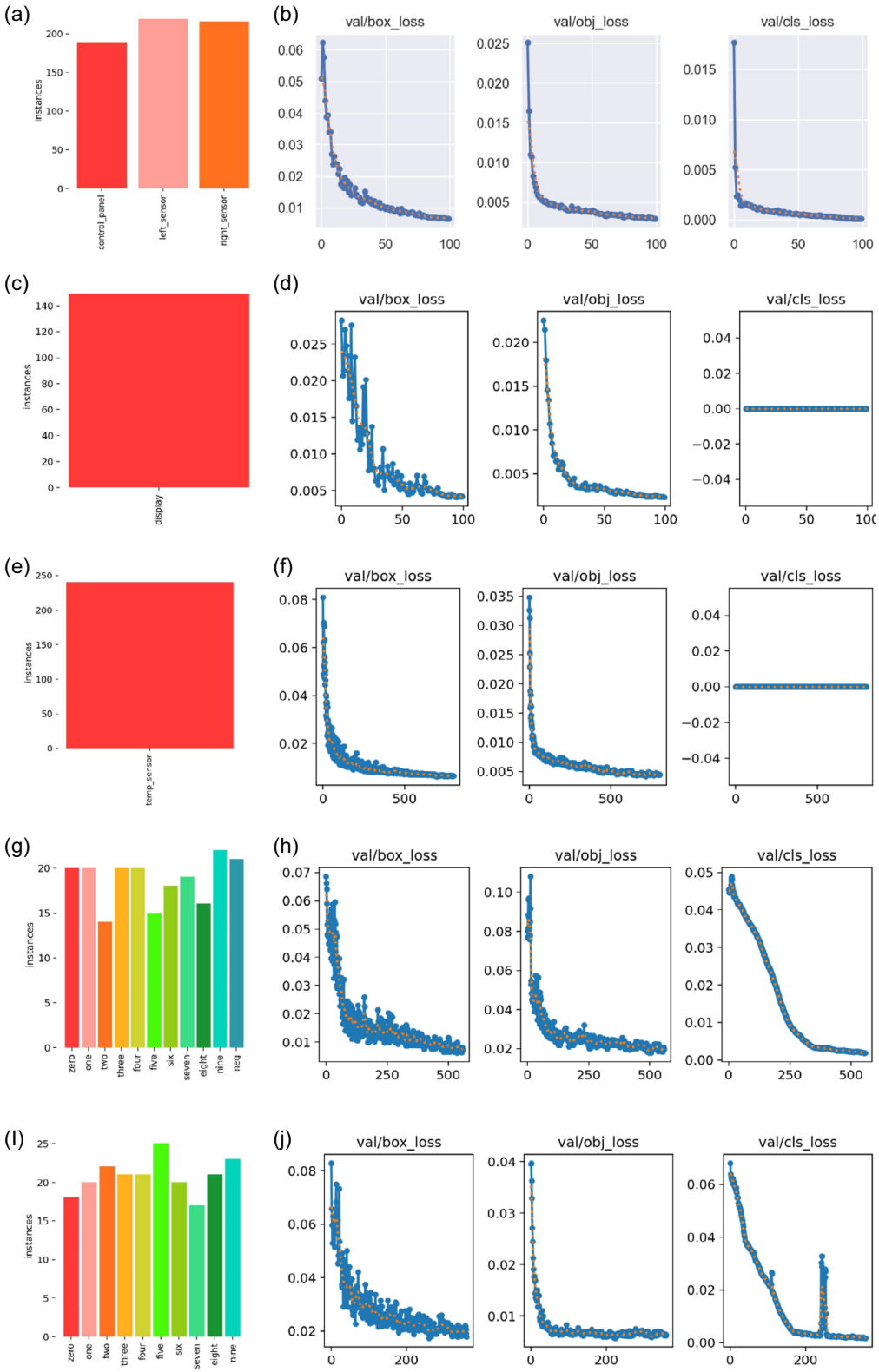

Figure 8. Distribution of the dataset along the different classes per model a) Machine Device model, c) Digital Micrometer Display, e) Temperature Display model, g) Micrometer Digits model, and i) LED Green Digits model. Loss function curve during the training of the validation dataset corresponding to b) Machine Device model, d) Digital Micrometer Display, f) Temperature Display model, h) Micrometer Digits model, and j) LED Green Digits model.

impact on the final porosity, which is reported in various studies.[46,49] However, the model does not accurately reflect the impact of temperature since there are very few parameter values to represent temperature. Reports indicate that calendering temperature has a considerable impact on the final porosity of the material.[19] The initial porosity has the second-highest absolute

Research Article
doi.org/10.1002/batt.202500292
Chemistry Europe
European Chemical Societies Publishing

Table 2. Optimal model hyperparameters for the random forest regressor model.

Model hyperparameters	
Maximum depth	6
Minimum samples at leaf	5
Minimum samples to split	12
No of estimators	180
Maximum features	0.8
Average model performance from Stratified K-fold Cross Validation	
Mean squared error	0.0004
R-squared	0.9575

average SHAP value. This value should mainly be contributed by data points with a low compression degree, but not so much when the compression degree is higher. Still, on average, a considerable effect is seen in the SHAP value. For example, let's compare a set of electrodes with the same formulation but with different initial porosity. When a compression degree of 30% is set, an electrode with an initial porosity value of 55% will experience lesser pressure than an electrode with an initial porosity of 40% since at the roll gap, the electrode with the lower initial porosity is closer to the minimum achievable porosity. The lesser pressure results in a lesser impact to the final electrode porosity according to the Heckel's equation.[46,49] The absolute average SHAP value of the parameters concerning the material properties, such as mass loading, initial porosity, and AM content, does not fully reflect their individual effects on the calendering process since they show multicollinearity in the dataset. It is important to understand that previous stages of the electrode manufacturing process (such as the drying stage) can have an effect on the calendering process.[47] Such effects mainly manifest in the material properties of the initial electrode before calendering and are also responsible for such multicollinearity (as in the case between mass loading and initial porosity). However, we can look at the combined effect of these features. By combining them, we can see that material properties are the second most impactful features after the effect of compression degree. While these limitations exist, our model sufficiently serves as a proof of concept for the approach we're demonstrating. The current analysis uses pre-existing data that was not specifically designed for this study, yet it still validates our concept effectively. With more targeted data collection, this approach could easily be expanded to address these limitations and provide even more comprehensive insights into the calendering process.

3.3. Defining the Calendering Process Tasks

We tested our solution with eight different users. For our testing, we defined a protocol along the calendering process to normalize and evaluate the performance of our solution. The protocol comprises three primary tasks: mobile phone interface, temperature setting, and digital micrometer settings. To begin with the test activity, a list of seven parameters (mass loading, active material content, initial thickness, upper temperature, lower temperature, right digital micrometer, and left digital micrometer) is established on a piece of paper prior to the use of the calendering machine and given to the user. Three of these seven parameters need to be set up in the mobile phone interface and the remaining four in the calendering machine itself.

The mobile phone interface task consists of entering the values of three parameters: mass loading (m_l) in mg cm^{-2}, active material content (AM_c) in weight fraction, and initial thickness (Th) in μm. The three values are inserted in the mobile phone interface by typing the desired numerical values. The type of active material is a drop down list, which is NMC 111 by default. Then, the manipulation of the calendering machine starts. In the temperature setting task, the user sets up the values (upper and lower temperature) for both temperature displays. Finally, the digital micrometer setting task takes place, where the user manipulates the hand wheels in front of the calendering machine

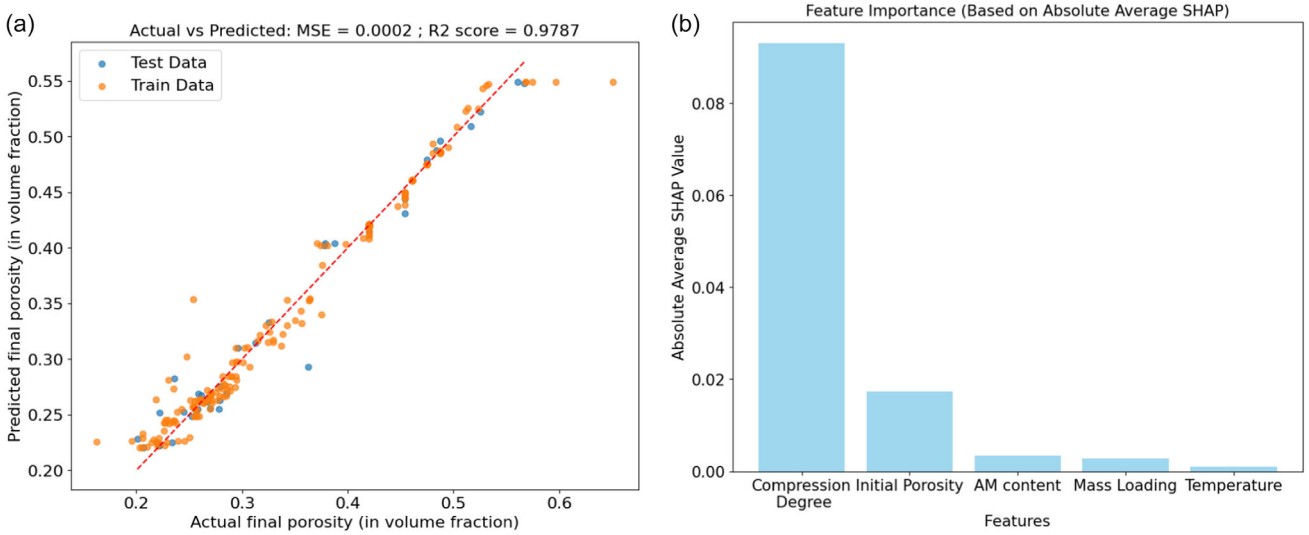

Figure 9. a) Predicted versus target plot of the final model. b) Graph representing absolute average SHAP value for different input parameters.

Research Article
doi.org/10.1002/batt.202500292
Chemistry Europe
European Chemical Societies Publishing

to set up the parameter values of both digital micrometers to their desired ones (left and right digital micrometers). During the whole process, the user can check that the values are being read correctly because they are being displayed in the holographic display in real time.

3.4. Computational Cost

We also conduct real-time performance testing to assess the computational cost of our solution during the operation of the HL App with our server. To analyze performance, we plot the wall time for each Process_Frame cycle, which is calculated by dividing the CPU time by the number of cores utilized. Our testing is performed on an i9 laptop that operates at 2.3 GHz and features 16 cores. This setup allows us to obtain a comprehensive understanding of the efficiency and responsiveness of our application under varying workloads, along with the manipulation of the calendering machine. In our analysis, we closely monitor the wall time required to complete one cycle of our Process_Frame function whenever a user engages with our solution.

For illustration, we have randomly selected the wall-time plots of three different users. To facilitate a more effective comparison of the task durations across different users, we have normalized the x-axis of our wall-time plots in terms of task completion (**Figure 10**). This normalization scales the timeline from 0 to 100%, where 0% indicates the start of the first task and 100% signifies the successful completion of all three tasks. This approach allows us to visualize and assess the relative time spent on each task in a standardized manner, irrespective of individual user variations. We can clearly observe the time distribution required for each of the three main tasks (mobile phone interface, temperature setting, roll gap setting). The most demanding task regarding the computational cost occurs during the red region, which corresponds to when the CV algorithm is capturing the temperature values from the display during user manipulation, having peaks of around one second per cycle. The second most demanding task regarding the computational cost is the blue region when the user is manipulating the hand wheels to change the value on the digital micrometers with a wall time of around 0.5 s per cycle.

3.5. Operational Test Results

To collect feedback from the eight users regarding their experience with our MR assistance solution, we implemented two assessment tools: the System Usability Scale (SUS)[50] questionnaire and the NASA Task Load Index (NASA-TLX)[51] questionnaire (Figure S5,S6, Supporting Information). The scores obtained from these two methodologies provide us with insights into how well our solution meets the needs of its end users. We have ensured a diverse group of testers, encompassing varying levels of experience, to evaluate our solution, which will help us understand its usability and overall user satisfaction (**Table 3**). By analyzing the results from both questionnaires, we aim to identify areas for improvement and gauge the effectiveness of our design from the perspective of different user categories.

For all eight test users, the initial conditions were meticulously standardized to ensure consistency in the testing of our digital

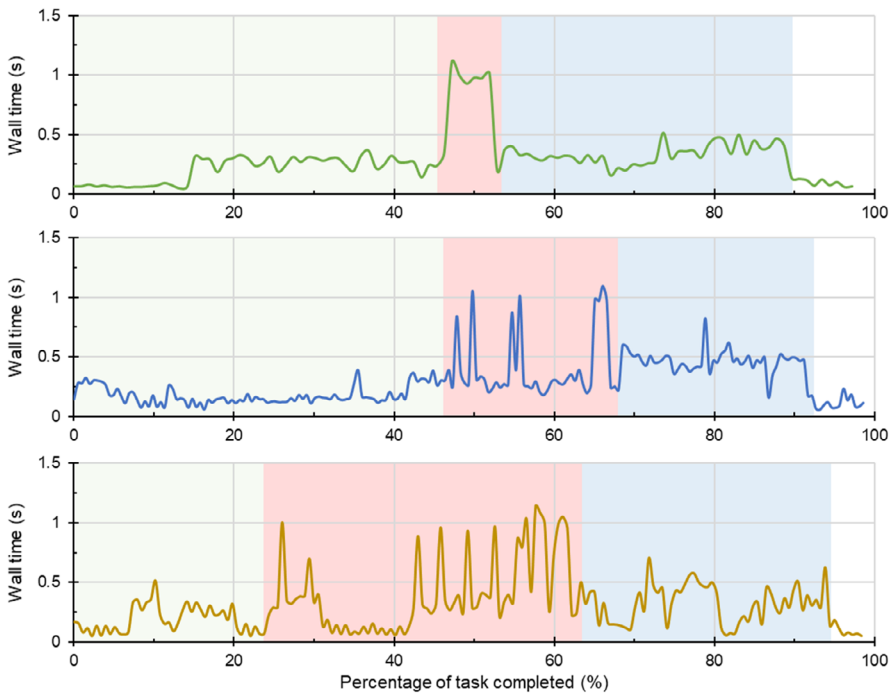

Figure 10. Wall time per cycle of our server computer when the HL app is running and the user is performing a calendering process with the machine. The plot shows the wall time per cycle of three different users. The green region corresponds to when the user is using the mobile phone interface. The red region corresponds to when the user is manipulating the temperature display. The blue region is when the user is manipulating the hand wheels to change the value of the digital micrometers.

Table 3. Operational test results and background information regarding the use of our MR assistant by all the test operators.

Operator ID	Process time without our digital assistant [s]	Process time with our digital assistant [s]				Operator background	Operator height [cm]
		Total	Mobile phone interface	Temperature setting	Micrometers setting		
1	84	132	41	24	67	Computational	167
2	88	280	175	36	69	Experimental	172
3	102	237	46	88	103	Experimental/ computational	186
4	104	193	42	58	93	Computational	180
5	106	196	49	78	69	Computational	180
6	139	243	48	97	98	Computational	194
7	140	245	46	93	106	Computational	191
8	70	310	31	112	167	Experimental/ Computational	175

assistant. At the beginning of the test, the mobile phone interface presented empty input boxes, allowing each user to enter their own numerical values. The calendering machine was configured to an initial temperature of 60 °C on both temperature displays, while the digital micrometers were calibrated to zero. Despite this uniform starting point, the three parameters that users were required to input (mass loading, active material content, and initial thickness) into the mobile phone interface varied among the participants. However, each user was tasked with adjusting the temperature display to a requested value of 62 °C—two degrees higher than the initial setting—and inputting a value of $-100\,\mu m$ in both digital micrometers. This controlled setup enabled an effective comparison of user interactions and responses. Additionally, during the testing, each user was isolated to ensure that their performance was not influenced by the presence of previous testers. This approach was implemented to maintain the integrity of the results and to provide accurate statistics on the usage of our MR assistant.

In general, without delving deeply into the analysis, we can observe that users who utilize our digital assistant tend to spend nearly twice the amount of time compared to those who do not use it (Table 3). However, it is important to consider that our digital assistant enables real-time predictions, which would otherwise require additional computational or experimental effort if performed manually. The primary advantage of our solution, therefore, lies in significantly reducing the time needed for such tasks, from several hours to just 2 min or less. To better understand how our digital assistant influences overall user performance, we also recorded the time each operator spent on the three specific tasks: mobile phone interface, temperature setting, and micrometers setting. This approach allows us to analyze not only the efficiency of task completion but also to identify patterns or anomalies that may indicate difficulties or advantages associated with the use of our MR assistant.

In our observations, most operators completed the mobile phone interface task in ≈40 s, demonstrating a relatively consistent performance. However, there was a notable exception: one operator took 175 s to complete the same task. Upon closer examination, we found that this extended duration was primarily due to the time spent by User 2 in initiating the HL App. This delay was mainly caused by difficulties in managing the holographic interface of the device, which hindered a smooth start-up process. Importantly, this prolonged time was not attributable to our digital assistant itself but rather to HL's interface challenges. This insight suggests that while our software may enhance performance, hardware and interface usability also play crucial roles in overall efficiency.

In our observations of the temperature setting and micrometers setting tasks, a clear pattern has emerged: the operation time required to complete these tasks is directly correlated with the height of the operator. Specifically, as the operator's height increases, the time taken to finish the temperature setting and micrometers setting tasks also tends to increase. This trend is evident regardless of whether the operator is using our digital assistant or not, indicating that the phenomenon is not solely attributable to our digital assistant's influence (Figure S7a, Supporting Information). Instead, it appears to be more related to the physical ergonomics involved in performing these tasks, such as manipulating the calendering machine. The impact of increased height is particularly significant in the temperature setting task, where the temperature displays are positioned at the center of the machine (Figure S7b, Supporting Information). Taller operators need to lean or reach further to see the display clearly, which adds to the overall operation time. Although the effect is less pronounced, it is still noticeable in the micrometers setting task, where operators are required to set up top digital micrometers. In this case, taller users may need to adopt more awkward postures or spend extra time adjusting their positioning to complete the setup efficiently (**Figure 11**a,b). Overall, these findings suggest that ergonomic factors related to operator height should be considered when designing or optimizing workflows to improve efficiency and reduce task completion times.

The SUS questionnaire consists of 10 questions (Figure S5, Supporting Information), with each designed to assess different aspects of usability. To calculate the score, responses to the questions are processed differently depending on whether the question number is odd or even. For each odd-numbered question, the score is obtained by subtracting 1 from the participant's response (score = response − 1). For each even-numbered question, the score is calculated by subtracting the response from 5

Research Article
doi.org/10.1002/batt.202500292
Chemistry Europe
European Chemical Societies Publishing

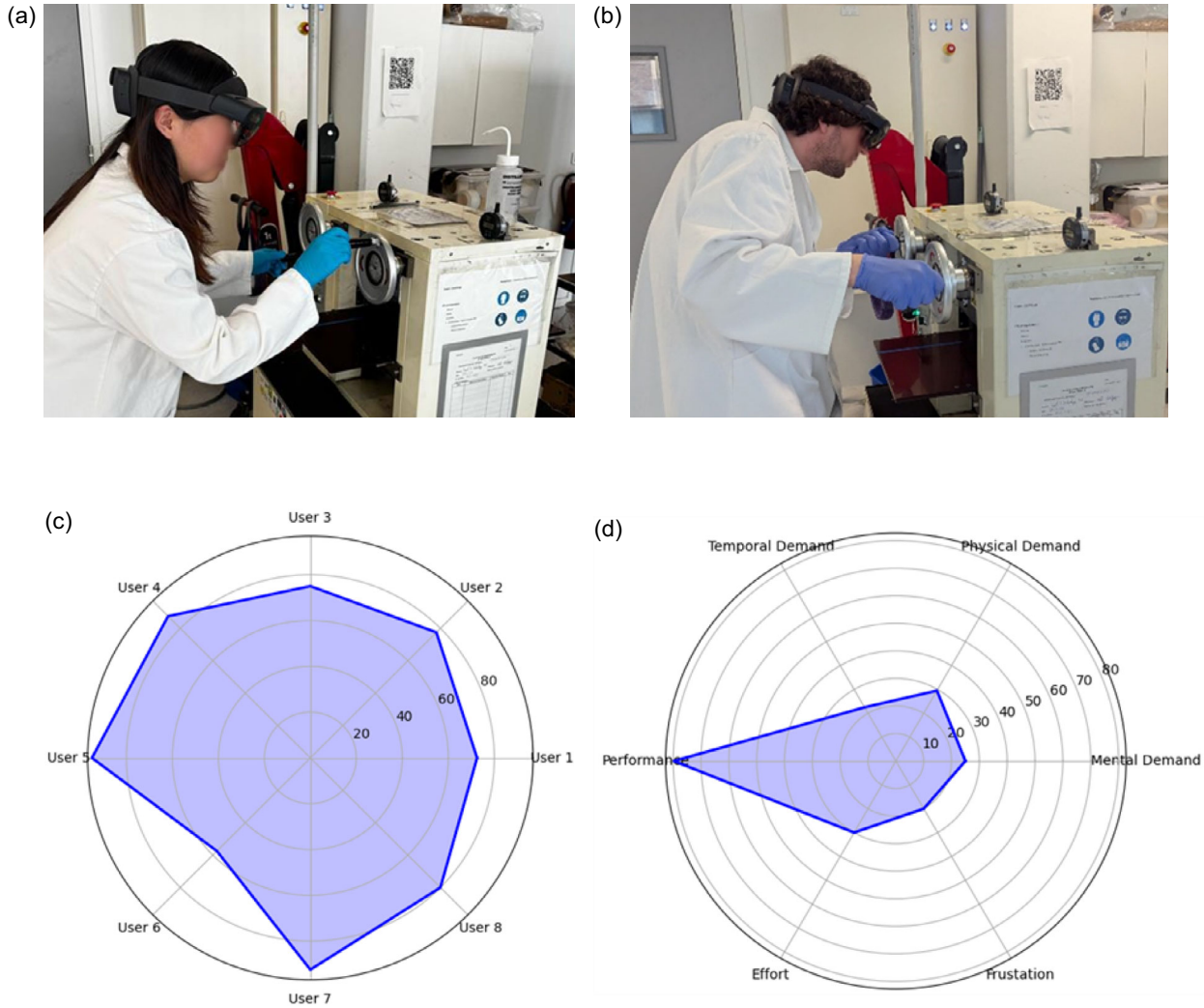

Figure 11. Different adopted positions by the users in order to make the CV algorithm read the digital micrometers values: a) 167 cm and b) 191 cm. c) SUS and d) NASA-TLX scores of the eight test users.

(score = 5-response). These individual item scores are then summed across all questions and multiplied by 2.5 to produce an overall SUS score that ranges from 0 to 100. The scores shown in the radar chart (Figure 11c) are the average SUS scores calculated per participant in the study.

The NASA-TLX score is calculated by having participants rate their perceived workload across six subscales: Mental Demand, Physical Demand, Temporal Demand, Performance, Effort, and Frustration Level (Figure S6, Supporting Information). Each subscale is rated on a scale typically ranging from low to high, and these ratings are then weighted based on the participant's perceived importance of each dimension. The weighted ratings are summed to produce an overall workload score, which ranges from 0 to 100, with higher scores indicating greater perceived workload. In the radar chart (Figure 11d), the scores displayed represent the average NASA-TLX scores calculated across all participants in the testing, providing a collective measure of perceived workload.

In general, and based on both radar chart scores, our digital assistant performance demonstrates consistently strong scores across all eight users, with values hovering around 80. This indicates a high level of user satisfaction and usability, reflecting a positive reception based on the SUS questionnaire results. Such uniformity in scores suggests that the system is well-received and performs reliably across different users, reinforcing its effectiveness and user-friendliness. Additionally, the NASA-TLX results indicate a high score on the Performance dimension, combined with very low scores on the other five workload categories (Mental Demand, Physical Demand, Temporal Demand, Effort, and Frustration), suggesting that users perceive the use of the digital assistant as highly successful or effective, with minimal perceived effort, stress, or difficulty. In an ergonomic context, this implies that our solution enables users to achieve the task efficiently and effectively. The low scores in the other dimensions indicate that the system does not impose significant mental or physical strain, nor does it induce frustration or temporal pressure, which are positive indicators of a well-designed, user-friendly solution. Overall, these findings support that our design optimally balances task demands with user capacity, promoting a comfortable and efficient interaction.

4. Summary and Outlook

In this article, we reported the development and implementation of an MR-supported digital assistant that leverages two key technologies: CV and ML. CV is employed to perceive and gather information about the environment, while ML processes this data to generate predictions. The system was tested in the context of the use of calendering manufacturing machinery, demonstrating its practical applicability. Importantly, our technology concept's core focus is on a modular workflow, which could be adapted to other industrial applications within the battery industry, making it a versatile solution for different operational scenarios.

Our MR-supported digital assistant workflow has demonstrated commendable effectiveness and aligns closely with our initial expectations. User feedback through the SUS and NASA-TLX questionnaires indicates that the MR assistant is intuitive and easy to use, making it accessible for individuals with different expertise. While it is acknowledged that the workflow can extend the time required to complete certain tasks, the real-time predictive capabilities offered by our ML model provide significant value. We used our ML regressor model to get a real-time porosity prediction. If we perform the task to predict the electrode porosity prior to or after the calendering process, in the traditional way as a mathematical calculation or via extensive computational physics-based simulations or additional experimental approaches, it leads to longer tasks. Therefore, the additional time investment in using our MR-supported digital assistant is justified by the efficiencies it introduces and its real-time predictive capability.

Furthermore, the modularity of our workflow is a standout feature, allowing for seamless adaptation to a variety of tasks. This flexibility not only enhances the potential for tailoring our MR-supported digital assistant tool to meet specific user needs but also opens the door to improving its predictive power by simply replacing the current ML model with a more sophisticated one, like a multidimensional regressor, which would be able to predict several electrode properties simultaneously. There are also improvement opportunities in terms of ergonomics. For example, users over 1.80 m tall may benefit from retraining the CV algorithm with diverse viewpoints. In the latter case, we anticipate enhanced performance without an increase in computational cost. The architecture of the CV model will remain intact, ensuring that the addition of more training samples can be integrated smoothly without altering the overall performance of the digital assistant. Another key aspect of our modular workflow design is its ability to integrate alternative interfaces, like a holographic add-on that can replace the mobile phone interface. This innovative approach eliminates the need for an additional device, such as a mobile phone, by embedding all essential features directly into our MR assistant through the holographic interface. Drawing on our prior work in developing holographic interaction systems,[12] we have demonstrated that data collection and user interaction can be effectively managed without reliance on conventional mobile devices. This modularity not only enhances user convenience and reduces device clutter but also offers a flexible platform adaptable to various user preferences and operational contexts.

Lastly, it is important to note that for several users in this study, this was their first experience with the HL hardware. Consequently, the time taken to complete tasks also includes the learning curve associated with operating the HL itself. As users become more familiar with the technology, we expect a reduction in the time required to complete tasks. Overall, the combination of user-friendly design, egocentric predictive capabilities, and adaptability postures of our MR-supported digital assistant is a valuable asset in enhancing productivity and efficiency in semi-manual activities in battery prototyping lines.

Acknowledgements

A.A.F. had the original idea of the human-centered digital assistant technology reported in this article. A.A.F., S.S., and D.E.G. acknowledge the funding support of the French National Research Agency under the France 2030 program (grant ANR-22-PEBA-0002, PEPR project "BATMAN"). A.A.F. deeply acknowledges the European Research Council for the funding support through the ERC Proof-of-Concept grant No. 101069244 (SMARTISTIC project). A.A.F. deeply acknowledges the European Union's Horizon 2020 research and innovation program for the funding support through the European Research Council (grant agreement 772873 ARTISTIC project). A.A.F. acknowledges the Institut Universitaire de France for the support. The authors acknowledge Romain Lelong (Reviatech SAS) for the implementation of the holographic panels in the HoloLens 2, subcontracted with the funding support of Prof. A.A. Franco's projects. The authors acknowledge the eight participants in the test sessions (in no particular order relative to Table 3): Pei Sun, Emmanuel Yerumoh, Hari Raj, Abhilash Valisammagari, Saad Ali, Victor Ramirez, Utkarsh Vijay, and Francisco Fernandez, all working in Prof. A.A. Franco's research group.

Conflict of Interest

The authors declare no conflict of interest.

Data Availability Statement

The data that support the findings of this study are available from the corresponding author upon reasonable request.

Keywords: artificial intelligence · battery prototyping · computer vision · real-time prediction · semi-manual manufacturing machinery

[1] Z. Zhang, S. S. Zhang, *Rechargeable Batteries: Materials, Technologies and New Trends*, Springer International Publishing, Cham **2015**.
[2] T. Kim, W. Song, D.-Y. Son, L. K. Ono, Y. Qi, *J. Mater. Chem. A* **2019**, *7*, 2942.
[3] S. S. Madani, Y. Shabeer, F. Allard, M. Fowler, C. Ziebert, Z. Wang, S. Panchal, H. Chaoui, S. Mekhilef, S. X. Dou, *Batteries* **2025**, *11*, 127.
[4] C. W. Babbitt, *Clean Technol. Environ. Policy* **2020**, *22*, 1213.
[5] S. Tagliapietra, G. Zachmann, O. Edenhofer, J.-M. Glachant, P. Linares, A. Loeschel, *Energy Policy* **2019**, *132*, 950.

[6] M. Fichtner, K. Edström, E. Ayerbe, M. Berecibar, A. Bhowmik, I. E. Castelli, S. Clark, R. Dominko, M. Erakca, A. A. Franco, A. Grimaud, B. Horstmann, A. Latz, H. Lorrmann, M. Meeus, R. Narayan, F. Pammer, J. Ruhland, H. Stein, T. Vegge, M. Weil, *Adv. Energy Mater.* **2022**, *12*, 2102904.
[7] L. Denisart, D. Zapata-Dominguez, X. David, A. Leclere, R. Lelong, C. Liu, J. Xu, E. Loup-Escande, A. A. Franco, *Batteries Supercaps* **2024**, *7*, e202300268.
[8] Home - i-MESC an Erasmus Mundus Joint Master, https://i-mesc.eu/ (accessed: April 2025).
[9] S. Saravanan, U. Vijay, S. Tran, M. M. Mathew, D. Y. Apostolova, I. Gandarias, A. Leclere, R. Lelong, A. A. Franco, *Batteries Supercaps* **2025**, e202500098.
[10] A. A. Franco, E. Loup-Escande, G. Loiseaux, J. N. Chotard, D. Zapata-Dominguez, J. Ciger, A. Leclere, L. Denisart, R. Lelong, *Batteries Supercaps* **2023**, *6*, e202200369.
[11] A. A. Franco, J. N. Chotard, E. Loup-Escande, Y. Yin, R. Zhao, A. Rucci, A. C. Ngandjong, S. Herbulot, B. Beye, J. Ciger, *Batteries Supercaps* **2020**, *3*, 1147.
[12] L. Denisart, J. F. Troncoso, E. Loup-Escande, A. A. Franco, *Batteries Supercaps* **2024**, *7*, e202400042.
[13] J. F. Troncoso, F. M. Zanotto, D. E. Galvez-Aranda, D. Zapata Dominguez, L. Denisart, A. A. Franco, *Batteries Supercaps* **2025**, *8*, e202400385.
[14] I. I. I. Wood, *J. Power Sources* **2015**, *275*, 234.
[15] O. Rynne, M. Dubarry, C. Molson, D. Lepage, A. Prébé, D. Aymé-Perrot, D. Rochefort, M. Dollé, *Batteries* **2019**, *5*, 72.
[16] R. P. Cunha, T. Lombardo, E. N. Primo, A. A. Franco, *Batteries Supercaps* **2020**, *3*, 60.
[17] M. Duquesnoy, T. Lombardo, M. Chouchane, E. N. Primo, A. A. Franco, *J. Power Sources* **2020**, *480*, 229103.
[18] M. Duquesnoy, I. Boyano, L. Ganborena, P. Cereijo, E. Ayerbe, A. A. Franco, *Energy AI* **2021**, *5*, 100090.
[19] E. N. Primo, M. Touzin, A. A. Franco, *Batteries Supercaps* **2021**, *4*, 834.
[20] M. Duquesnoy, T. Lombardo, F. Caro, F. Haudiquez, A. C. Ngandjong, J. Xu, H. Oularbi, A. A. Franco, *npj Comput. Mater.* **2022**, *8*, 161.
[21] A. Shodiev, M. Duquesnoy, O. Arcelus, M. Chouchane, J. Li, A. A. Franco, *J. Power Sources* **2021**, *511*, 230384.
[22] A. El Malki, M. Asch, O. Arcelus, A. Shodiev, J. Yu, A. A. Franco, *J. Power Sources Adv.* **2023**, *20*, 100114.
[23] D. E. Galvez-Aranda, F. Fernandez, A. A. Franco, *ACS Appl. Mater. Interfaces* **2025**, *17*, 32150.
[24] D. E. Galvez-Aranda, T. L. Dinh, U. Vijay, F. M. Zanotto, A. A. Franco, *Adv. Energy Mater.* **2024**, *14*, 2400376.
[25] F. Fernandez, S. Saravanan, R. L. Omongos, J. F. Troncoso, D. E. Galvez-Aranda, A. A. Franco, *npj Adv. Manuf.* **2025**, *2*, 14.
[26] M. Duquesnoy, C. Liu, D. Z. Dominguez, V. Kumar, E. Ayerbe, A. A. Franco, *Energy Storage Mater.* **2023**, *56*, 50.
[27] M. Duquesnoy, C. Liu, V. Kumar, E. Ayerbe, A. A. Franco, *J. Power Sources* **2024**, *590*, 233674.
[28] M. Sonzogni, J.-M. Vanson, Y. Reynier, S. Martinet, K. Ioannidou, F. Radjai, *Powder Technol.* **2024**, *442*, 119891.
[29] M. Lippke, T. Ohnimus, F. Frankenberg, C. Schilde, A. Kwade, *Powder Technol.* **2024**, *444*, 119984.
[30] M. F. Niri, C. Reynolds, L. A. R. Ramírez, E. Kendrick, J. Marco, *Energy Storage Mater.* **2022**, *51*, 223.
[31] S. Haghi, J. Keilhofer, N. Schwarz, P. He, R. Daub, *Batteries Supercaps* **2024**, *7*, e202300457.
[32] F. M. Zanotto, D. Z. Dominguez, E. Ayerbe, I. Boyano, C. Burmeister, M. Duquesnoy, M. Eisentraeger, J. F. Montaño, A. Gallo-Bueno, L. Gold, F. Hall, N. Kaden, B. Muerkens, L. Otaegui, Y. Reynier, S. Stier, M. Thomitzek, A. Turetskyy, N. Vallin, J. Wessel, X. Xu, J. Abbasov, A. A. Franco, *Batteries Supercaps* **2022**, *5*, e202200224.
[33] Z. Ren, Z. Ren, Z. Zhang, T. Buonassisi, J. Li, *Nat. Rev. Mater.* **2023**, *8*, 563.
[34] G. Tom, S. P. Schmid, S. G. Baird, Y. Cao, K. Darvish, H. Hao, S. Lo, S. Pablo-García, E. M. Rajaonson, M. Skreta, *Chem. Rev.* **2024**, *124*, 9633.
[35] D. P. Tabor, L. M. Roch, S. K. Saikin, C. Kreisbeck, D. Sheberla, J. H. Montoya, S. Dwaraknath, M. Aykol, C. Ortiz, H. Tribukait, *Nat. Rev. Mater.* **2018**, *3*, 5.
[36] A. A. Volk, M. Abolhasani, *Nat. Commun.* **2024**, *15*, 1378.
[37] O. Bayley, E. Savino, A. Slattery, T. Noël, *Matter* **2024**, *7*, 2382.
[38] L. Hung, J. A. Yager, D. Monteverde, D. Baiocchi, H.-K. Kwon, S. Sun, S. Suram, *Digital Discovery* **2024**, *3*, 1273.
[39] N. Choudhary, H. Clever, R. Ludwigs, M. Rath, A. Gannouni, A. Schmetz, T. Hülsmann, J. Sawodny, L. Fischer, A. Kampker, *Adv. Intell. Syst.* **2022**, *4*, 2200142.
[40] M. Zorn, C. Ionescu, D. Klohs, K. Zähl, N. Kisseler, A. Daldrup, S. Hams, Y. Zheng, C. Offermanns, S. Flamme, *Recycling* **2022**, *7*, 48.
[41] M. Johnson, A. Khatoon, Fitzpatrick, C. In *2022 Inter. Conf. on Electrical, Computer, Communications and Mechatronics Engineering (ICECCME)*, IEEE, Piscataway, NJ **2022**, pp 1–6.
[42] Q. Yu, L. Xiao, D. Zheng, Z. Peng, K. Song, *Trans. China Weld. Inst.* **2024**, *45*, 38.
[43] P. Bhavsar, A. Dutta, S. K. Pal, *Meas. Sci. Technol.* **2024**, *35*, 085407.
[44] G. Bradski, *Dr. Dobb's J.: Software Tools Prof. Programmer* **2000**, *25*, 120.
[45] J. Redmon, S. Divvala, R. Girshick, A. Farhadi, In *2016 IEEE Conf. Computer Vision and Pattern Recognition*, CVPR, Las Vegas, NV, USA **2016**, pp. 779–788.
[46] E. N. Primo, M. Chouchane, M. Touzin, P. Vazquez, A. A. Franco, *J. Power Sources* **2021**, *488*, 229361.
[47] D. Z. Dominguez, B. Mondal, M. Gaberscek, M. Morcrette, A. A. Franco, *J. Power Sources* **2023**, *580*, 233367.
[48] F. Pedregosa, G. Varoquaux, A. Gramfort, V. Michel, B. Thirion, O. Grisel, M. Blondel, P. Prettenhofer, R. Weiss, V. Dubourg, J. Vanderplas, A. Passos, D. Cournapeau, M. Brucher, M. Perrot, É. Duchesnay, *J. Mach. Learn. Res.* **2011**, *12*, 2825.
[49] C. Meyer, M. Kosfeld, W. Haselrieder, A. Kwade, *J. Energy Storage* **2018**, *18*, 371.
[50] J. R. Lewis, *Int. J. Human–Comput. Interact.* **2018**, *34*, 577.
[51] J. M. Noyes, D. P. Bruneau, *Ergonomics* **2007**, *50*, 514.

Manuscript received: April 18, 2025
Revised manuscript received: June 4, 2025
Version of record online: